INTERNATIONAL JOURNAL FOR NUMERICAL METHODS IN FLUIDS
Int. J. Numer. Meth. Fluids 2006; **50**:1207–1228
Published online 28 December 2005 in Wiley InterScience (www.interscience.wiley.com). DOI: 10.1002/fld.1152

MPDATA and grid adaptivity in geophysical fluid flow models

J. M. Prusa[1,*,†] and W. J. Gutowski[2,‡]

[1]*Department of Mechanical Engineering, Iowa State University, Ames, IA 50011, U.S.A.*
[2]*Department of Geological and Atmospheric Sciences, Iowa State University, Ames, IA 50011, U.S.A.*

SUMMARY

Geophysical flows can profoundly affect human activities. Often characterized by an astonishing range of significant scales and a rich assortment of physical processes, the complexity of such flows generally precludes all but numerical simulation for prediction and understanding—yet even state of the art computational models may be severely challenged by problems such as hurricane intensification. Although a number of significant issues are involved, a major factor is often grid resolution, for which *grid adaptivity* (GA) can be useful. Our experience has been that MPDATA is particularly well suited for GA. This paper sketches general details of a model that blends MPDATA with continuous GA; highlights a tensor viewpoint of the geometric conservation law; and presents results for both global and regional atmospheric applications. Together, the examples demonstrate the advantages of using GA with MPDATA to resolve fine-scale features—explicit gravity waves generated by flow over orography. Resolution of these waves (or lack thereof) are shown to affect global climate; furthermore, wave resolution is shown to depend upon the regional atmospheric environment. Finally the regional simulations show a surprising increase in the complexity of the wavefields as resolution is increased to the point of resolving nonhydrostatic effects. Copyright © 2005 John Wiley & Sons, Ltd.

KEY WORDS: MPDATA; grid adaptivity; continuous mappings; geophysical flows

1. INTRODUCTION

Historically, a primary focus in attempting to solve problems with a large range of scales has been the development of simplifying approximations such as sub-grid physical parameterizations (e.g. turbulence, micro-physics, convection, etc. [1–4]), simplified analytical models

*Correspondence to: J. M. Prusa, Teraflux Corporation, Boca Raton, FL, 33486, U.S.A.
†E-mail: jprusa@bellsouth.net
‡E-mail: gutowski@iastate.edu

Contract/grant sponsor: U.S. Department of Energy; contract/grant numbers: DEFG0296ER61473, DEFG0201ER63250
Contract/grant sponsor: U.S. National Center for Atmospheric Research
Contract/grant sponsor: U.S. National Science Foundation

Received 30 March 2005
Revised 3 October 2005
Accepted 7 November 2005

Copyright © 2005 John Wiley & Sons, Ltd.

(e.g. incompressible, hydrostatic, anelastic, etc. [5, 6]), more efficient computational algorithms (e.g. implicit methods, multigrid, etc. [7, 8]); and improved machine hardware (e.g. faster processors, parallel processors, etc.) to greatly reduce the range of scales and CPU time necessary to simulate a geophysical flow problem on a given processor. Indeed, the cumulative effect of software advances on top of hardware advances appears to follow an extended form of Moore's law in which software advances approximately match hardware advances in improving the performance of large computational models [9]. Although the cumulative improvement has been of the order of 10^5 during the past 20 years, accurate simulations of problems such as global climate continue to severely tax state of the art computational models [10]. Even regional short-term forecasts can be problematic. A clear example occurs in hurricane prediction where very unanticipated behaviours are possible.[1] To the extent that grid resolution is a limiting factor in simulations such as these, *grid adaptivity* (GA) can help close the gap between the need for better accuracy and what current technology can offer.

Grid adaptivity describes a wide variety of methods for locally increasing grid resolution in computational models in regions of interest. Such methods include nested grids, grid point insertion/deletion, and redistribution methods, among others [12]. In this study, the focus is on the redistribution of continuous coordinates. Compared to other types of GA, our method tends to be analytically challenging, and somewhat less capable of adapting to highly convoluted geometrical shapes; but it offers very high efficiency[2] and the power of tensor theoretic methods to help ensure the consistency of the model equations. When coupled with MPDATA, our resultant computational model, *EULAG*, routinely yields conservation properties accurate to 4–6 significant figures (generally this is limited only by the degree of convergence of pressure, which can in principle be driven to machine precision)—a quality that is important for long time integrations such as are needed for climate simulation (see Reference [14] for vorticity diagnostics and Section 3.1 of this study for vorticity and continuity diagnostics). Finally, we note that *EULAG* can work equally well with analytically specified or numerically generated grids [13]; and can handle step changes in grid resolution that mimic nested grids without producing spurious Gibb's oscillations or other noise (see Reference [15] for background history, and Reference [13] and Section 3.2 of this study to substantiate our claim).

Although the deformable grid capability of our model is 'relatively' mature, the development of dynamic grid generators for geophysical flows is still in comparative infancy. While *targets*[3] for grid adaptation are relatively straightforward in more elementary applications such

[1] In September 2004, Hurricane Jeanne executed a sudden trajectory change due north from the northern edge of Haiti, and then a clockwise loop some seven degrees north of the Dominican Republic before taking on a straight westward trajectory into southern Florida. The 48 h forecast trajectories by an ensemble of models published by the National Hurricane Center *all* missed predicting this 'detour' in an overall WNW trajectory into the state of Florida [11].

[2] In practice changes in CPU time depend upon the physics of the resulting solutions; there is only relatively minor overhead from the GA machinery itself. Generally, the CPU time is dictated by Courant number stability and for such cases scales like $\sim \Delta t^{-1}$. It is possible that the CPU time *decrease* with GA, should the pressure equation become sufficiently better conditioned as a result of GA, see Reference [13] and Section 3.1 of this study.

[3] By *target* we mean the structures in the solution and/or computational domain to which the grid is adapted.

Copyright © 2005 John Wiley & Sons, Ltd.

as in flows past topography[4] [16–19]; free surface flows[5] [25]; or in tracer transport[6] [12, 28]; it is not at all clear how to adapt in more complicated applications such as climate prediction. In climate the targeting choices for adaptation are far more varied. Major geographical features such as mountain ranges, valleys, and coastlines provide stationary targets for grid adaptation; simultaneously wind, temperature, and water vapor fields provide dynamic ones. The strategy utilized may depend strongly on the information desired, e.g. effects of mesoscale convection, baroclinic eddies, tropical storms, orographic forcing, or—as will be shown later in Section 3.2—nonhydrostaticity. The choices of scales and physical phenomena for targeting are many.

In the following section we highlight some of the analytical and numerical details of the computational model. With the exception of material in Section 2.3, the presentation presents only a light sketch of the model details. All of the relevant details both numerical and analytical have been previously published in the archival literature, here for purposes of focus and space we give ample citations for the interested reader. In Section 2.3, we present, we believe, a new more fundamental tensor based proof of a general conservation principle of considerable importance in GA. Although long recognized as being important, our tensor based form of this *purely geometrical* constraint reveals considerable new insights as to what must be satisfied and how it can be done. This new formalism has led to excellent results in simulations with GA [13, 14, 25]. Finally, in Section 3 we show results from idealized global and regional flows with idealized orographic forcing. GA makes possible the resolution of orographic wave forcing in the global simulation. The regional simulations are made primarily to substantiate the global results. However the fine scale ($\sim$10 km) nonhydrostatic effects that appear make this example an excellent one to showcase the advantages of the combination of the NFT solver MPDATA, GA and tensor formalism underlying our model. These attributes make it readily able to resolve to sub-kilometer scales and show fine scale nonhydrostatic effects even though the computational domain must be large enough to capture strong forcing with a characteristic horizontal scale of $\sim$500 km.

2. THE COMPUTATIONAL MODEL

Our anelastic, nonhydrostatic computational model is based upon a synergism between a non-Cartesian tensorial representation of the model equations and nonoscillatory-forward-in-time (NFT) numerical schemes [5, 13, 14, 25]. We implement GA capability via rigorous application of a continuous mapping from an orthogonal curvilinear system of coordinates describing a space $\mathbf{S}_p$—where the physical problem is posed—into a transformed system of coordinates describing a new space $\mathbf{S}_t$. The physical problem is solved in the transformed system utilizing the NFT Eulerian method, MPDATA [29].[7] The synergy arises because the tensorial

[4] When topography is present, it provides a clear geometric disturbance to the flow that requires high local resolution to resolve wave activity near the topography.

[5] Historically, free surface flows and other problems characterized by irregular and/or moving domain boundaries provided the impetus for the initial development of numerical grid adaptation, [20–24].

[6] Targeting various combinations of the tracer magnitude, gradient and/or second derivatives of the tracer field have all produced good results [19, 26, 27].

[7] An NFT semi-Lagrangian method [30] is also a model option.

Copyright © 2005 John Wiley & Sons, Ltd.

description helps in generating computational forms in generalized (transformed) coordinates that maintain important properties of the solution. In particular, conservation depends upon a geometric conservation law (GCL) which is expressed as a tensor identity in Section 2.3. From a numerical perspective, not all analytical forms are equally useful, and some forms result in much more efficacious computational models. Our experience is that solving the model equations in standard tensor form is not the best choice for the model, and instead use a blend of various contravariant, covariant, and physical forms. The NFT character of MPDATA brings additional benefits. For example, although formally the coordinate mapping must be C^2 continuous, the model can accommodate mappings with step discontinuities—that is, a nested grid—without introducing refractions/reflections from the sudden change in grid resolution (see Reference [13] and Section 3.2 below).

A few comments about notation are in order. Although we use conventional operator notation in Section 2.2, throughout Sections 2.1 and 2.3 the preferred notation is tensor. Wherever indices are repeated as upper and lower indices a summation over all values of that index is implied unless specifically noted otherwise (there *are* exceptions). Some indices range over the spatial coordinates only, others include time. Finally, we use the symbols $\equiv$ to mean *identically equal to*, $:=$ to mean *defined as*, and $\sim$ to mean *approximately equal to*.

2.1. Analytical formulation

We formulate (and solve) the governing equations in transformed coordinates $(\bar{t},\bar{x},\bar{y},\bar{z})$ that describe a computational domain $\mathbf{S}_t$. The coordinates (t,x,y,z) for the physical domain $\mathbf{S}_p$ are assumed orthogonal and stationary—Cartesian or spherical are typical examples. The physical domains admitted under the diffeomorphism

$$(\bar{t},\bar{x},\bar{y},\bar{z}) := (t, E(t,x,y), D(t,x,y), C(t,x,y,z)) \tag{1}$$

cover a range from the canonical Cartesian box, to spherical shells with irregular undulating boundaries. The following paragraphs highlight only a few key issues, for a more comprehensive treatment the reader is referred to References [13, 31].

Given (1) the anelastic equations of Reference [32] can be written as

$$\frac{\partial(\rho^* \overline{v^s}^k)}{\partial \bar{x}^k} = 0 \tag{2}$$

$$\frac{\mathrm{d}v^j}{\mathrm{d}\bar{t}} = -\tilde{G}^k_j \frac{\partial \pi'}{\partial \bar{x}^k} + g\frac{\theta'}{\theta_b}\delta^j_3 + \mathscr{F}^j + \mathscr{V}^j \tag{3}$$

$$\frac{\mathrm{d}\theta'}{\mathrm{d}\bar{t}} = -\overline{v^s}^k \frac{\partial \theta_e}{\partial \bar{x}^k} + \mathscr{H} \tag{4}$$

While these model equations may at first appear traditional, they are a hybrid form that blends physical and tensor forms. They retain the *coordinate invariance* of a full tensor formulation and are also complete in the sense that no approximations have been utilized other than the anelasticity, and that $\mathbf{S}_p$ is intrinsically 'flat', e.g. has a zero Riemann curvature tensor[8] and is described by an orthogonal system of coordinates.

[8]The Riemann curvature tensor measures the curvature of the space–time underlying $\mathbf{S}_p$, and is distinct from and does not rule out the case of curved spaces such as a spherical shell in an underlying Euclidean space.

Copyright © 2005 John Wiley & Sons, Ltd.

Briefly, v^j denote components of the *physical velocity*[9] defined in $\mathbf{S}_p$; θ, ρ, and π denote potential temperature, density, and a density-normalized pressure; g is the acceleration of gravity; $\mathscr{F}^j$ symbolizes the deviation of inertial forces (e.g. Coriolis and geospherical metric accelerations) from the geostrophically balanced ambient (or environmental) state v_e^j, θ_e; whereas $\mathscr{V}^j$ symbolizes viscous dissipation of momentum; and $\mathscr{H}$ denotes diffusion and sources/sinks of heat. Primes denote perturbations with respect to the environmental state, and the subscript b refers to the basic state, i.e. a horizontally homogeneous hydrostatic reference state of a Boussinesq type expansion around a constant stability profile; $\rho^* := \rho_b \bar{G}$, where $\bar{G}$ denotes the Jacobian of the transformation, and $j,k = 1,2,3$ correspond to 'x', 'y', 'z' components, respectively, in either $\mathbf{S}_p$ or $\mathbf{S}_t$. In the momentum equation (3) $\tilde{G}_j^k := \sqrt{g^{jj}}(\partial \bar{x}^k/\partial x^j)$ are renormalized elements of the Jacobi matrix where summation is not implied over j, and δ_3^j is the Kronecker delta. The coefficients g^{jj} are the diagonal elements of the conjugate metric tensor of $\mathbf{S}_p$. The total derivative is given by $\mathrm{d}/\mathrm{d}\bar{t} = \overline{v^*}^i(\partial/\partial \bar{x}^i)$, where $\overline{v^*}^i$ is the *contravariant velocity* in $\mathbf{S}_t$, and $\overline{v^s}^i$ appearing in continuity (2) is the *solenoidal* velocity in $\mathbf{S}_t$. These two velocities differ from each other by the grid speeds and are distinct from the physical velocities. The indices $i,m = 0,1,2,3$; and $i,m = 0$ refer to time $\bar{t}$, with $\overline{v^*}^0 \equiv 1$. The *covariant velocity* $\overline{v^*}_i$ is required for evaluating the strain rate tensor appearing in $\mathscr{V}^j$.

2.2. Numerical method

The theory and performance of our NFT approach have been broadly documented in the literature; see Reference [33] for a succinct review. In essence, we approximate the prognostic equations (3) or (4) to second-order accuracy in space and time, employing a formal congruency of the Eulerian [29] and semi-Lagrangian [30] optional model algorithms. Either algorithm can be written in the compact form

$$\psi_{\mathbf{i}}^{n+1} = \mathrm{LE}_{\mathbf{i}}(\tilde{\psi}) + 0.5\Delta t R_{\mathbf{i}}^{n+1} := \hat{\psi}_{\mathbf{i}} + 0.5\Delta t R_{\mathbf{i}}^{n+1} \tag{5}$$

where $\psi_{\mathbf{i}}^{n+1}$ is the solution sought at the grid point $(\bar{t}^{n+1}, \bar{\mathbf{x}}_{\mathbf{i}})$, $\tilde{\psi} := \psi^n + 0.5\Delta t R^n$, and R represents forcings (diffusion, buoyancy, sources/sinks, and so on) for prognostic equations according to the Lagrangian form $\mathrm{d}\psi/\mathrm{d}\bar{t} = R$. The numerical operator LE denotes a two-time-level advective semi-Lagrangian or flux-form Eulerian NFT transport operator. In the Eulerian scheme, LE integrates a homogeneous transport equation for $\tilde{\psi}$ using a fully second-order-accurate multidimensional NFT advection scheme [29]; whereas in the semi-Lagrangian algorithm, LE remaps transported fields, which arrive at the grid points $(\bar{t}, \bar{\mathbf{x}}_{\mathbf{i}})$, back to the departure points of the flow trajectories $(\bar{t}^n, \bar{\mathbf{x}}_o(\bar{t}^{n+1}, \bar{\mathbf{x}}_{\mathbf{i}}))$ also using NFT advection schemes [30]. Equation (5) represents a system of equations that is implicit with respect to all dependent variables in (3) and (4), since all forcing terms are assumed to be unknown at $n+1$. Note that the forcing term on the rhs of (4) contains the complete convective derivative. This is significant because it guarantees that the implicitness of the numerical approximation does not adversely affect either the impermeability of the lower boundary or the conservation of θ', regardless of details of the transformation (1) (see Reference [5]).

[9] In meteorological applications, the physical velocity is typically defined using a local Cartesian system and so has dimensions of length/time.

Copyright © 2005 John Wiley & Sons, Ltd.

The implicitness of the pressure gradient forces is an essential feature of the anelastic model, as it enables the projection of the preliminary values LE($\tilde{\psi}$) onto solutions of the continuity equation (2). To make this projection, the system of simultaneous equations resulting from (5) are algebraically inverted to construct expressions for the solenoidal velocity components. These components are substituted into (2) to produce the elliptic pressure equation:

$$-\frac{\Delta t}{\rho^*}\frac{\partial}{\partial \bar{x}^j}\left[\rho^* \mathscr{E}\left(\tilde{\mathscr{V}}^j - \tilde{\mathscr{C}}^{jk}\frac{\partial \pi'}{\partial \bar{x}^k}\right)\right] = 0 \tag{6}$$

where the entire equation has been premultiplied by $-\Delta t/\rho^*$—a normalization that gives the residual errors of (6) the sense of the divergence of a dimensionless velocity on the grid. This facilitates the design of physically meaningful stopping criteria for the pressure solver [34]. The factor (-1) assures the formal negative-definiteness of the elliptic operator on the lhs of (6), required for convergence of the pressure solver. The coefficients $\mathscr{E}$, $\tilde{\mathscr{V}}^j$, and $\tilde{\mathscr{C}}^{jk}$ are complicated functions of the reference state, computational parameters, Coriolis accelerations, and the dependent fields. A complete exposition is given in Reference [13].

The elliptic pressure equation (6) is solved (subject to appropriate boundary conditions) using the generalized conjugate-residual approach—a preconditioned nonsymmetric Krylov-subspace solver [35, 36]. Given the updated pressure, and hence the updated solenoidal velocity,[10] the updated physical and contravariant velocity components are constructed from the solenoidal velocities (details may be found in Reference [13]). Nonlinear terms in R^{n+1} (e.g. metric terms arising on the globe) may require outer iteration of the system of equations generated by (5)—see Appendix of Reference [5] for discussion. Additional details and references for sub-grid-scale modelling and moisture may be found in Reference [33].

2.3. The geometric conservation law as a tensor identity

Early in the development of GA it was recognized that the method of computation of metric terms appeared to have significant impact on conservation properties, even for numerical schemes that were conservative in a Cartesian formulation. Starting from first principles, Thomas and Lombard [21] determined that if the Jacobian $\bar{G}$ of the transformation[11] satisfied a certain prognostic equation, termed the GCL, that the volume of the transformed computational domain would be properly preserved. Currently, the GCL is recognized as being an important property of computational models with GA [37]. Here we depart from attempts to satisfy the GCL through use of an additional prognostic equation and instead show that the GCL is a tensor identity, and that it may be satisfied by computing requisite metric terms utilizing other standard tensor identities.

The tensor form of the GCL may be motivated by transforming any conservation law from one coordinate system to another via the chain rule. If the law is written in tensor form, then the transformed law must retain identical structure due to the coordinate invariance property of tensor forms. The actual computation, however, will reveal a residual term exists [14, 31],

[10] $\mathscr{E}(\tilde{\mathscr{V}}^j - \cdots)$ in (6) is the updated solenoidal velocity $\overline{v^{s^j}}|^{n+1}$.

[11] Here $\bar{G} = |\bar{g}_{mn}|^{1/2}$ where $\bar{g}_{mn} = g_{pq}(\partial x^p/\partial \bar{x}^m)(\partial x^q/\partial \bar{x}^n)$ denotes the metric tensor of $\mathbf{S}_t$ and g_{pq} denotes the metric tensor of $\mathbf{S}_p$.

Copyright © 2005 John Wiley & Sons, Ltd.

with a coefficient equal to the left-hand side of

$$\frac{G}{\bar{G}}\frac{\partial}{\partial \bar{x}^i}\left(\frac{\bar{G}}{G}\frac{\partial \bar{x}^i}{\partial x^m}\right) \equiv 0 \tag{7}$$

The coefficient is set to zero because tensor invariance requires it. The left-hand side of (7) can be recognized as the divergence in $\mathbf{S}_t$ of the form $(1/G)\partial \bar{x}^i/\partial x^m$ multiplied by the Jacobian of $\mathbf{S}_p$. This form gives weighted 'velocities' ($m=0$), or 'stretching factors' ($m=1,2,3$) between $\mathbf{S}_p$ and $\mathbf{S}_t$. Evidently (7) is a set of four independent statements about the *conservation of space*. It is the tensor form of the GCL.

In order to recognize that (7) contains the more traditional form of the GCL, consider the $m=0$ component when $\mathbf{S}_p$ is described by Cartesian coordinates. Then $x^m=t$ and $G\equiv 1$, and (7) reduces to

$$\frac{\partial \bar{G}}{\partial \bar{t}} + \frac{\partial}{\partial \bar{x}}\left(\bar{G}\frac{\partial \bar{x}}{\partial t}\right) + \frac{\partial}{\partial \bar{y}}\left(\bar{G}\frac{\partial \bar{y}}{\partial t}\right) + \frac{\partial}{\partial \bar{z}}\left(\bar{G}\frac{\partial \bar{z}}{\partial t}\right) \equiv 0 \tag{8}$$

This is exactly Equation (12) in Reference [21]. Satisfaction of (8) does *not* guarantee that the $m=1,2,3$ components of (7) are satisfied, however.

In practice, we interpret and utilize the GCL quite differently from that implied by the form (8). First, we expand and reorganize (7) into the computationally *more useful* form:

$$\frac{G}{\bar{G}}\frac{\partial}{\partial x^m}\left(\frac{\bar{G}}{G}\right) \equiv -\frac{\partial}{\partial \bar{x}^i}\left(\frac{\partial \bar{x}^i}{\partial x^m}\right) \tag{9}$$

Now it is clear that the GCL provides a connection between the derivatives of the Jacobian and derivatives of the elements of the Jacobi matrix. This form is also equivalent to the transformation law for contracted Christoffel symbols (proven below). As an example of implementation, consider the time variable extension [18] of terrain following coordinates [16]. Then the Jacobian $\bar{G}=GG_o$ where G and $G_o=(H-z_s)/H$ are the Jacobians of $\mathbf{S}_p$ and of terrain following coordinates in Cartesian coordinates, respectively. The surface mapping function is denoted $z_s(t,x,y)$ and H is a constant domain height. In this case, (9) results in:[12]

$$G_o^{-1}\frac{\partial G_o}{\partial x^m} = -\frac{\partial C_{,x^m}}{\partial \bar{z}} = \begin{cases} -z_{s,x^m}/(H-z_s), & m=0,1,2 \\ 0, & m=3 \end{cases} \tag{10}$$

Here subscripts preceded by a comma denote partial derivatives. Only the $C_{,x^m}$ for $m=0,1,2,3$ are required in the computational model. Since $C_{,z}=G_o$ by definition, and $C_{,x^m}=-z_{s,x^m}(H-\bar{z})/(H-z_s)$ for $m=0,1,2$; (10) is viewed as providing computational formulae for computing the z_{s,x^m}—and not the derivatives of G_o.

In the more general case of horizontal stretching [13] and/or more complicated vertical stretching [25], the GCL in the form (9) is still used to determine the metric terms $C_{,x^m}$. Although extra terms appear in (10), fundamentally it retains the same structure. But this is

[12]Note that the Jacobian of the orthogonal coordinates describing $\mathbf{S}_p$ does not enter into (10). This is one of the advantages of using non-Cartesian tensors; Equation (10) has exactly the same form whether $\mathbf{S}_p$ is described by Cartesian, spherical, toroidal, etc. coordinates.

Copyright © 2005 John Wiley & Sons, Ltd.

not the complete story. The four components of the GCL cannot directly provide guidance relating all the additional metric coefficients that arise in the more general transformations, and one may ask—are such relationships needed? The answer is a *most emphatic* yes!

The key to understanding what additional relations need to be satisfied is found by proving (7) via purely geometrical arguments. Following Reference [31], we begin by setting the left-hand side of (7) equal to a residual $\mathscr{R}$ and by direct expansion and tensor manipulations, prove $\mathscr{R} \equiv 0$. Expanding (7) and reorganizing terms yields:

$$\mathscr{R} \equiv \left(\frac{1}{\bar{G}}\frac{\partial \bar{G}}{\partial \bar{x}^i}\right)\frac{\partial \bar{x}^i}{\partial x^m} + \frac{\partial x^n}{\partial \bar{x}^i}\frac{\partial}{\partial x^n}\left(\frac{\partial \bar{x}^i}{\partial x^m}\right) - \left(\frac{1}{G}\frac{\partial G}{\partial x^n}\right)\left(\frac{\partial x^n}{\partial \bar{x}^i}\frac{\partial \bar{x}^i}{\partial x^m}\right) \tag{11}$$

In the first term, the parenthetical expression may be replaced with a contracted Christoffel symbol of the second kind in $\mathbf{S}_t$, using the identity:

$$\overline{\left\{ \begin{matrix} n \\ n \quad i \end{matrix} \right\}} \equiv \frac{1}{\bar{G}}\frac{\partial \bar{G}}{\partial \bar{x}^i} \tag{12}$$

cf. Section 2.5 in Reference [38]. In the third term, the derivative of G has been expanded using the chain rule, and regrouped into two parenthetical expressions. The first one can again be rewritten as a contracted Christoffel symbol of the second kind, only now in $\mathbf{S}_p$. The second expression is recognized, via the identity

$$\delta^n_m \equiv \frac{\partial \bar{x}^n}{\partial x^i}\frac{\partial x^i}{\partial \bar{x}^m} \tag{13}$$

to be the Kronecker delta tensor ($n, m = 0, 1, 2, 3$). Clearly n must be set equal to m in this third term. After relabelling dummy (repeating) indices, there results:

$$\mathscr{R} \equiv \overline{\left\{ \begin{matrix} n \\ n \quad i \end{matrix} \right\}}\frac{\partial \bar{x}^i}{\partial x^m} + \frac{\partial x^n}{\partial \bar{x}^i}\frac{\partial^2 \bar{x}^i}{\partial x^n \partial x^m} - \left\{ \begin{matrix} n \\ n \quad m \end{matrix} \right\} \tag{14}$$

The proof is now completed by writing the transformation law for Christoffel symbols of the second kind, and contracting the upper index to one of the lower ones. The details are tedious but standard, resulting in

$$\left\{ \begin{matrix} n \\ n \quad m \end{matrix} \right\} \equiv \left(\frac{\partial \bar{x}^o}{\partial x^n}\frac{\partial x^n}{\partial \bar{x}^l}\right)\frac{\partial \bar{x}^i}{\partial x^m}\overline{\left\{ \begin{matrix} l \\ o \quad i \end{matrix} \right\}} + \frac{\partial x^n}{\partial \bar{x}^o}\frac{\partial^2 \bar{x}^o}{\partial x^n \partial x^m} \tag{15}$$

The range of indices for l, o are $0, 1, 2, 3$. In the first term on the right, the parenthetical expression is recognized to be another Kronecker delta, so o must be set equal to l in this term. Then l becomes a dummy index in the transformed Christoffel symbol and may be relabelled n. In the second term on the right, o is a dummy index and so may be relabelled i. The right-hand side of (15) is now recognized to be *exactly* the first two terms on the right-hand side of (14) and we have the desired result $\mathscr{R} \equiv 0$.

In summary, satisfying the GCL requires only the rigorous application of standard tensor operations and identities. The most germane identities are the relationship between elements of the Jacobi and inverse Jacobi matrices (13), and the transformation rule for contracted Christoffel symbols (Equation (14) with $\mathscr{R} \equiv 0$). The former requires that care must be taken in how various metric terms are computed, and the latter that care must be taken in

Copyright © 2005 John Wiley & Sons, Ltd.

how the derivatives of various metric terms are computed. The transformation rule for contracted Christoffel symbols leads immediately back to (9);[13] thus only (13) provides something new. In four-dimensional space–time, (13) consists of 16 simultaneous equations—differential identities—that relate the elements of the Jacobi and inverse Jacobi matrices of the transformation from $\mathbf{S}_p$ to $\mathbf{S}_t$. Given our specified functional form for transformation (1), six of these reduce to trivial statements (i.e. $0=0$ or $1=1$), leaving 10 equations relating 20 metric coefficients. These equations can be utilized on a 'need to use' basis. Since the problem is solved in $\mathbf{S}_t$, the physical coordinates of $\mathbf{S}_p$ are treated as dependent variables, that is, $x^i = x^i(\bar{x}^m)$. Once the $\partial x^i/\partial \bar{x}^m$ have been determined (either analytically or numerically), the simultaneous equations (13) are used to determine the inverse metric coefficients $\partial \bar{x}^m/\partial x^i$—which is what are required in the $\tilde{G}^k_j$ coefficients that appear throughout the model. In practice, the use of the differential identities is limited to the metric coefficients that are not already specified by (9). For the case of no horizontal stretching (13) is irrelevant, whereas for cases with horizontal stretching it is critically important in maintaining the tensor form of the GCL (7).[14] Our experience to date is that using (9) and (13) as needed to evaluate metric terms gives excellent results [13, 14, 25].

3. RESULTS AND DISCUSSION

3.1. Idealized global simulation with idealized Andes topography

This example was designed to test GA in the context of a global simulation, with the specific goal of attempting to resolve orographically forced gravity waves and to assess possible impacts on climate statistics. The computational model was set up to simulate the idealized Held–Suarez climate [39] over a topography representing an idealization of the Andes mountains of South America.

The Andes, orientated roughly north to south, are noteworthy because of their extreme height, with a large number of peaks exceeding 6000 m from $-35°$ to $-10°$ of latitude. Numerous peaks over 4000 m extend from $-45°$ to $+5°$ degrees. Thus they rise nearly half a scale height into the troposphere over half of the latitudinal extent of the southern hemisphere. Clearly there is a potential for them to significantly impact the mean flows, yet the mountain range is narrow in east to west extent, typically no more than 500 km. This presents a severe constraint on climate models if they are to resolve the orographic forcing caused by these mountains. Here we idealize the topography of the Andes as a long narrow, NS oriented ridge. The topography is the analytically specified profile

$$z_s(x, y) = A \exp\left\{ - \left[\left(\frac{x - x_o}{\sigma_x} \right)^2 + \left(\frac{y - y_o}{\sigma_y} \right)^2 \right]^2 \right\} \tag{16}$$

[13] To see this, set $\mathscr{R} \equiv 0$ in (14), and apply (12) to rewrite the Christoffel symbols as derivatives of the Jacobian. The first and middle terms can be reorganized to eliminate derivatives with respect to $\bar{x}^i$ and x^n, respectively. The first and third terms may then be combined, resulting in the form (9).

[14] Given the ubiquity with which (13) appears in standard tensor operations, its use to relate the Jacobi and inverse Jacobi elements likely has numerous ramifications.

Copyright © 2005 John Wiley & Sons, Ltd.

where $A = 5000\,\mathrm{m}$ is the peak height, centred at $x_o = 180^\circ$ longitude[15] and $y_o = -20^\circ$ latitude. The peak half widths are $\sigma_x = 2.5^\circ$ and $\sigma_y = 25^\circ$.

Three simulations using a grid size of $(128 \times 64 \times 41)$ nodes in the (zonal $\times$ meridional $\times$ vertical) directions, respectively, were made. The first and second simulations, denoted G1 and G2, used a uniform grid corresponding to a resolution of $2.83^\circ, 2.81^\circ, 0.75\,\mathrm{km}$ in the zonal, meridional and vertical coordinates,[16] respectively. Simulation G2 differs from G1 by incorporating the idealized Andes topography (16)—simulation G1 uses a surface of constant radius. The third simulation, denoted G3, also incorporates this topography, but in addition uses horizontal GA to more finely resolve the local region about the topography.[17] The horizontal GA was analytically specified using a mapping similar to the one specified in Section 4 of Reference [13] with maximum longitudinal and meridional stretching factors of $S_x = 3$ and $S_y = 2$, respectively. The centre of maximum resolution was set over the topography, and so was stationary. Figure 1 depicts the effect of this GA in that it effectively 'magnifies' the topography so it may be better resolved by the computational model (note that the coordinate lines shown in Figure 1 represent a coarser resolution than used in the simulation in order to better show the stretching effects). The uniform grid results used a timestep of 450 s, whereas 360 s was used for the third case with GA. The initial wind fields were zero, as in Reference [13]. The simulations were computed for 480 days, with 'climate' statistics being computed using the second 240 day interval.

Table I summarizes the computational cost of the global simulations, as well as measures of two conservation properties. In column three observe that the CPU time *decreases* with the use of GA—a 21% reduction for G3 vs G2. This is due to a decrease in the condition number of the pressure solver [13]. The last two columns show, after 480 days of integration, extreme values and the global average values of two fields that should be identically zero. The first of these fields is the flow divergence, DVF, given by the solenoidal continuity equation (2). The values in Table I are multiplied by the timestep even though this increases their magnitudes by nearly three orders because the normalized value is more appropriate for gauging the accuracy of the solution [34]. Since (2) is the basis of our elliptic pressure equation (6), the flow divergences can be driven down to machine precision simply by increasing the number of pressure iterations. The second field is the divergence of the solenoidal vorticity multiplied by the timestep, $\mathrm{DVV} := \nabla \cdot \omega^s \Delta t$. It is a well-known vector identity that the divergence of the curl of a vector field must be identically zero. In generalized coordinates, the vorticity must be expressed as a contravariant form since this is what the generalized divergence operator requires. Given our coordinate mapping (1), this simplifies to the divergence of the *solenoidal* vorticity which is defined similarly to the solenoidal velocity (see References [14, 31] for the development of generalized vorticity). The extreme values in column four are measures of greatest local departure from these identities. They are due to the truncation error of the solutions. The global average fields are much smaller. These results are routine for our model with a pressure convergence stopping criterion of 0.3×10^{-4}.

[15]Since there is only one topographical feature and the surface is otherwise uniform, the longitudinal location is arbitrary.

[16]The model atmosphere has a depth of 30 km.

[17]Compared to simulation G2, there is no change in vertical resolution; however compared to G1 there is a change corresponding to the effect of terrain following coordinates [16].

Copyright © 2005 John Wiley & Sons, Ltd.

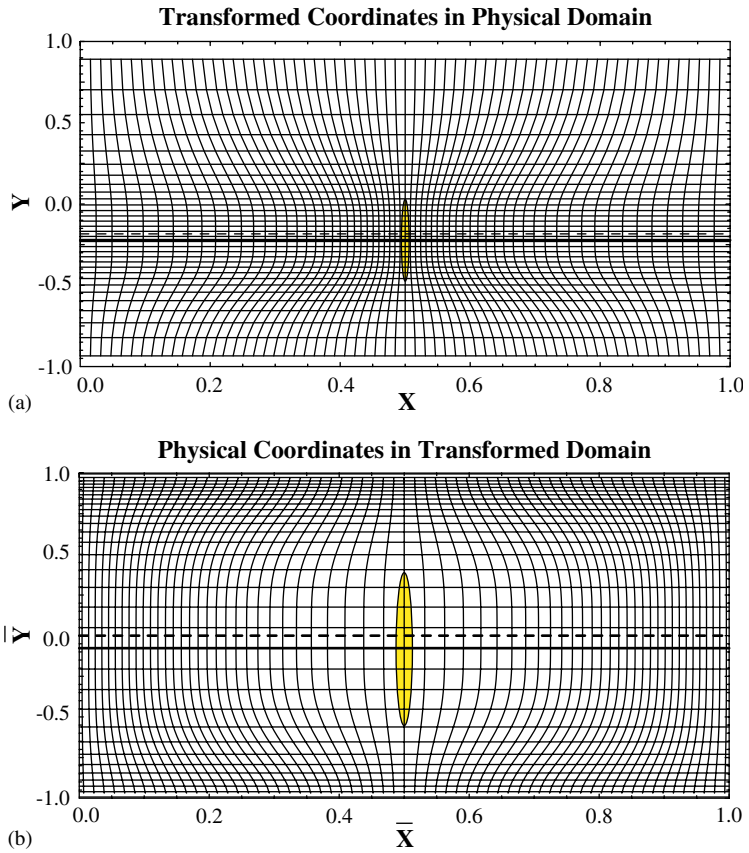

Figure 1. Representative continuous mapping for global simulation in normalized coordinates. $(X,\bar{X}) = (\lambda,\bar{\lambda})/360^\circ$, $(Y,\bar{Y}) = (\phi,\bar{\phi})/90^\circ$, where (λ,ϕ) are the zonal and meridional coordinates, respectively. The shaded in ellipsoid shows approximate extent of idealized topography. Bold solid line shows latitude of maximum meridional resolution and bold dashed line shows latitude of centre of transformed meridional coordinate $\bar{Y}$.

Table I. Summary of global simulations.

Simulation	Type	CPU time	Ext(DVF, DVV)	Ave(DVF, DVV)
G1	Uniform	0.86	$(1.32, 3.49) \times 10^{-5}$	$(7.62, 0.20) \times 10^{-8}$
G2	Uniform	1.00	$(3.63, 44.9) \times 10^{-5}$	$(-40.5, -0.80) \times 10^{-9}$
G3	Continuous	0.79	$(7.92, 4.84) \times 10^{-5}$	$(1.66, 2.60) \times 10^{-9}$

Type refers to the stretching used for the horizontal grid; CPU time is relative time to compute 120 days of simulated time, with simulation G2 requiring 26.7 h wall clock time on 16 POWER 3 PE's of the IBM RS/6000 cluster Blackforest at the U.S. National Center for Atmospheric Research; DVF is the flow divergence normalized by timestep, $\nabla \cdot (\rho^* \mathbf{v}^s)\Delta t$, and DVV is the divergence of solenoidal vorticity normalized by timestep, $\nabla \cdot \omega^s \Delta t$; $\mathrm{Ext}(A,B) := (\mathrm{Ext}(A), \mathrm{Ext}(B))$ and $\mathrm{Ave}(A,B) := (\mathrm{Ave}(A), \mathrm{Ave}(B))$ where $\mathrm{Ave}(A)$ is the average and $\mathrm{Ext}(A) := \mathrm{Max}[\mathrm{Max}(A), |\mathrm{Min}(A)|]$.

Copyright © 2005 John Wiley & Sons, Ltd.

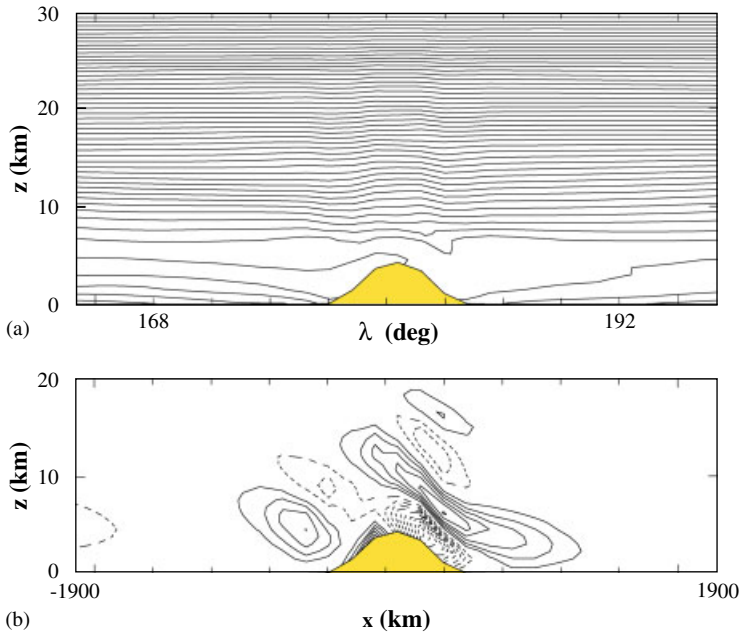

Figure 2. Local xz fields from global simulation G3 at latitude $\phi = -35.5^\circ$ latitude. Approximate zonal extent of 35° (3800 km) centred on southern flank of idealized topography: (a) natural log of potential temperature field at 298.75 days; min $= 5.625$ (277 K) at bottom, max $= 6.500$ (665 K) at top, inc $= 0.0175$ (4.8 K at bottom increasing to 11.6 K at top); and (b) vertical wind field at 299.00 days; $(\min, \max, \text{inc}) = (-0.17, 0.11, 0.02)\,\text{ms}^{-1}$.

Simulation G1 replicates the standard Held–Suarez climate and compares well with previously published results [5, 13, 39]. Although somewhat similar to the first simulation, G2 shows: (i) a loss of symmetry between the northern and southern hemispheres; (ii) a weakened and somewhat distorted southern midlatitude zonal jet; and (iii) strong westerlies at higher altitudes in the equatorial zone. A weaker southern jet is supported by climate statistics [40] for equinox conditions (which are more representative of the Held–Suarez forcing). However, the strong westerlies at upper equatorial altitudes are anomalous.

With up to three times the local resolution of G2—that is, 0.94° zonal $\times\, 1.41^\circ$ meridional—simulation G3 is capable of directly resolving larger gravity waves. Figure 2 clearly shows such an instance along the southern flank of the Andes at $\phi := y/R_o = -35.5^\circ$ latitude near day 299 (R_o is the planetary radius). The details of the wavefield shown in the localized xz slices of Figure 2 change appreciably on a time scale of 1 day, and are also quite sensitive to latitude. Nevertheless, horizontal and vertical wavelengths of $\lambda_x = 550$ and $\lambda_z = 10$ km, respectively, are typical in the region above 7.5 km altitude. These wave characteristics can be shown to fit the dispersion equation for inertio-gravity waves (a generalization based upon Equation (5.7) in Reference [13]) to within 15%. It is noteworthy that no such clear examples of waves occurred in G2 which used the uniform grid.

Figure 3 shows the zonal-time average of zonal wind for G2 and G3. The most significant difference between the two 'climates' is that the anomalous equatorial jet apparent in Figure 3(a) does not appear in Figure 3(b). We attribute this difference solely to the influence

Copyright © 2005 John Wiley & Sons, Ltd.

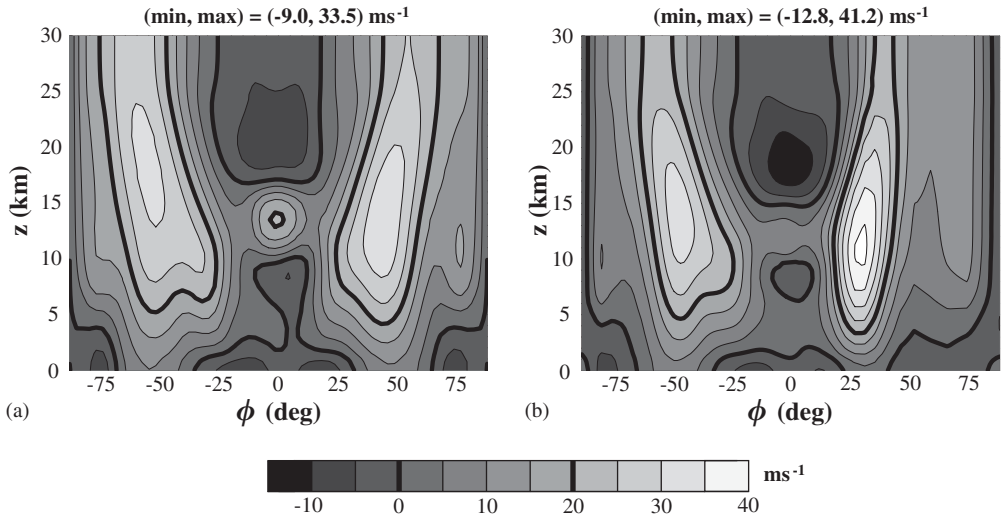

Figure 3. Global simulation zonal-time averages of the zonal wind, u. The zonal averaging is global; the time averaging is over the 240 day interval from 240 to 480 days: (a) simulation G2, horizontally uniform grid with idealized Andes topography; and (b) simulation G3, idealized topography with horizontal GA that selectively targets the topography.

of insufficiently resolved orographic wave forcing. Details behind this assertion are given in the following subsection. We close our discussion of the global results by observing that the northern jet in Figure 3(b) is stronger, narrower, and shifted equatorward compared to Figure 3(a). These traits are characteristic of poor meridional resolution [13]. In fact, at the northern jet centre $\phi = 30°$ latitude, the local resolution is 4.3°, or only 65% of the meridional resolution of G2. This contrasts sharply with the enhanced meridional resolution in the southern hemisphere. This example serves to point out that the selection of targets and grid generation algorithms have to be made with considerable finesse.

3.2. Idealized regional simulation with idealized Andes topography

The comparisons in the previous subsection suggest that by resolving inertio-gravity waves over the idealized topography, more realistic 'climate' results. But it does not elucidate the details of the wave-forcing mechanism by which this may occur. In this section, we utilize the model in regional mode to investigate the effects of resolution on regional wave forcing. Additionally, we highlight some additional GA mappings which allow us to readily resolve to sub-km scale even though the computational domain is thousands of km in zonal extent. We find that as resolution increases to $\sim$10 km and beyond, that the wave field dramatically alters character compared to Figure 2 due to nonhydrostatic effects.

A series of 2D simulations with zonal resolutions ranging from a low of 315 km—corresponding to the uniform grid in global simulation G2—to a maximum of 0.890 km were conducted. All regional simulations used the same vertical resolution and domain depth as in the global simulations as well as a zonal extent of $\sim$35° and the topographic profile generated by (16) at $-35.5°$ latitude as shown in Figure 2. Since the primary focus of these

Copyright © 2005 John Wiley & Sons, Ltd.

simulations was to assess the effects of zonal resolution, Coriolis effects were set to zero.[18] The environmental potential temperature field was set to match that of the global Held–Suarez forcing at -35.5° latitude; the same basic state density field was also used. The environmental zonal wind field was set equal to the 48 h average value from global simulation G3 for days 297.0–299.0. This average was also a regional one over the domain $163^\circ \leqslant \lambda \leqslant 198^\circ$ (3800 km zonal extent at -35.5° latitude) and $-38.8^\circ \leqslant \phi \leqslant -32.8^\circ$ (670 km meridional extent); where $\lambda := x/R_o$. The resulting averaged wind fields indicate the local environment has a zonal wind that is one of constant shear rate $\gamma = 0.0019\,\mathrm{s}^{-1}$ from the surface up to $\sim$12 km altitude. It peaks at a value of $25.0\,\mathrm{ms}^{-1}$ at $\sim$13.5 km, and then decreases with a constant shear rate of $\gamma = -0.0030\,\mathrm{s}^{-1}$ to near zero values at $\sim$22.5 km altitude and above. The averaged meridional wind for the local environment is $\sim$5 times smaller than the averaged zonal wind and so was assumed identically zero. The averaged vertical wind for the local environment is $\sim 0.01\,\mathrm{ms}^{-1}$ and thus completely negligible.

A 3D simulation at intermediate zonal resolution was also made to assess the impact of spanwise disturbances. This run used a meridional extent of 300 km, a uniform $\Delta y = 7.5$ km, and continuous GA in the zonal direction. The continuous mapping was specified by

$$X(\bar{X} : S_x, X_o) = X_o + S_x^{-1}(\bar{X} - \bar{X}_o) + \left\{ \frac{(1 - S_x^{-1})(\bar{X} - \bar{X}_o)^5}{1 + 10\bar{X}_o^2 + 5\bar{X}_o^4} \right\} \tag{17}$$

where $S_x(t)$ is the maximum stretching factor at location $X = X_o(t)$ in the normalized physical coordinates of $\mathbf{S}_p$, and $\bar{X} = \bar{X}_o(\bar{t})$ is the corresponding location in the normalized transformed coordinates of $\mathbf{S}_t$. Required is that $X_o \in [-1, +1]$, since this is the domain and range of the mapping.[19] Generally, time adaptation enters the mapping implicitly through these two parameters. Constant values of $S_x = 2.857$ and $X_o = 0.1053$ were used in this simulation, corresponding to a maximum zonal resolution of $\Delta x = 7.00$ km at $x = 200$ km (right flank of topography). The value of $\bar{X}_o$ is best determined iteratively from

$$X_o = 1 - S_x^{-1}(1 - \bar{X}_o) - \left\{ \frac{(1 - S_x^{-1})(1 - \bar{X}_o)^5}{1 + 10\bar{X}_o^2 + 5\bar{X}_o^4} \right\} \tag{18}$$

The continuous mapping (17) has the additional property of zero second derivative at the point of maximum stretching. This ensures that the Jacobian is nearly constant for an extended neighbourhood of the targeted region.

Table II summarizes the regional simulations, designated as R1–R10, with R10 being the 3D simulation. Higher resolution 2D runs R8, R9 also used the continuous GA mapping (17), but with $S_x = 2.801$ (and the same X_o). Simulation R7 used the 'nested' GA mapping

$$X(\bar{X} : S_x, X_o) = \begin{cases} G_1 & \forall \bar{X} \in [-1, \bar{X}_L] \\ G_1 + G_2 & \forall \bar{X} \in (\bar{X}_L, \bar{X}_R] \\ G_1 + G_2 + G_3 & \forall \bar{X} \in (\bar{X}_R, +1] \end{cases} \tag{19}$$

[18] The dispersion equation for inertio-gravity waves quantifies this effect as being of the order of 10% on wave characteristics such as wavelengths.

[19] This mapping is for computational domains with open boundary conditions. For an example appropriate for periodic boundary conditions, see Section 4 of Reference [13].

Copyright © 2005 John Wiley & Sons, Ltd.

Table II. Summary of regional simulations.

Simulation	$\Delta x : n$	Type	Δt	CPU time	I_{EF}
R1	315 : 13	Uniform	900	—	−0.121
R2	122 : 32	Uniform	360	0.006	−0.165
R3	50.0 : 77	Uniform	240	0.03	−0.42
R4	20.0 : 191	Uniform	180	0.1	−0.64
R5	7.0 : 543	Uniform	90	1	−0.69
R6	2.5 : 1521	Uniform	45	9	−0.79
R7	2.5 : 543	Nested	45	2	−0.78
R8	2.5 : 543	Continuous	45	1.4	−0.79
R9	0.890 : 1521	Continuous	20	25	−0.79
R10 (3D)	7.0 : 191	Continuous	120	29	−0.75

Δx in km; n is number of gridpoints; Δt in s; CPU time is relative time to compute to 720 min simulated time, with simulation R5 requiring 159 s on a single POWER 4 PE of the IBM RS/6000 cluster Bluesky at the U.S. National Center for Atmospheric Research; and integrated eddy flux ($\mathrm{J/m^2}$), I_{EF}, is the column integrated vertical eddy flux (see discussion of Figure 6). For simulations with GA (either nested or continuous) Δx gives the maximum resolution in the target region. For the 3D simulation, R10, 41 spanwise nodes were used with a constant $\Delta y = 7.5$ km.

where

$$\begin{aligned} G_1(\bar{X} : S_x, X_o) &= -1 + S_x^{-1}\Gamma(\bar{X} + 1) \\ G_2(\bar{X} : S_x, X_o) &= -S_x^{-1}(\Gamma - 1)(\bar{X} - \bar{X}_L) \\ G_3(\bar{X} : S_x, X_o) &= S_x^{-1}(\Gamma - 1)(\bar{X} - \bar{X}_R) \end{aligned} \tag{20}$$

As in (17), $S_x(t)$ is the enhancement in resolution over that of a uniform grid, and $X_o(t)$ is the centre of the target region in normalized physical coordinates. The remaining parameters are defined as follows:

$$\begin{aligned} \Gamma &= (S_x - \bar{X}_l)/(1 - \bar{X}_l) \\ \bar{X}_o &= \bar{X}_l - 1 + (1 + X_o - S_x^{-1}\bar{X}_l)/(S_x^{-1}\Gamma) \\ \bar{X}_L &= \bar{X}_o - \bar{X}_l \\ \bar{X}_R &= \bar{X}_o + \bar{X}_l \end{aligned} \tag{21}$$

where $\bar{X}_l$ is the fraction of the transformed coordinates alloted to the high resolution 'nest'; and $\bar{X}_L, \bar{X}_o, \bar{X}_R$ are the left edge, centre, and right edge of the high resolution region in normalized transformed coordinates, respectively. Generally, $\bar{X}_l = 0.30$ works well.[20] In simulation R7, $S_x = 2.801$ and $X_o = 0.1053$ were used so as to match the continuous GA of R8. This nested GA

[20]Large values of $\bar{X}_l$ cause the outer grid to have quite poor resolution, while small values make the nested region too small. Care has to be taken in implementing (19)–(21) so that both of $\bar{X}_L, \bar{X}_R \in [-1, +1]$.

Copyright © 2005 John Wiley & Sons, Ltd.

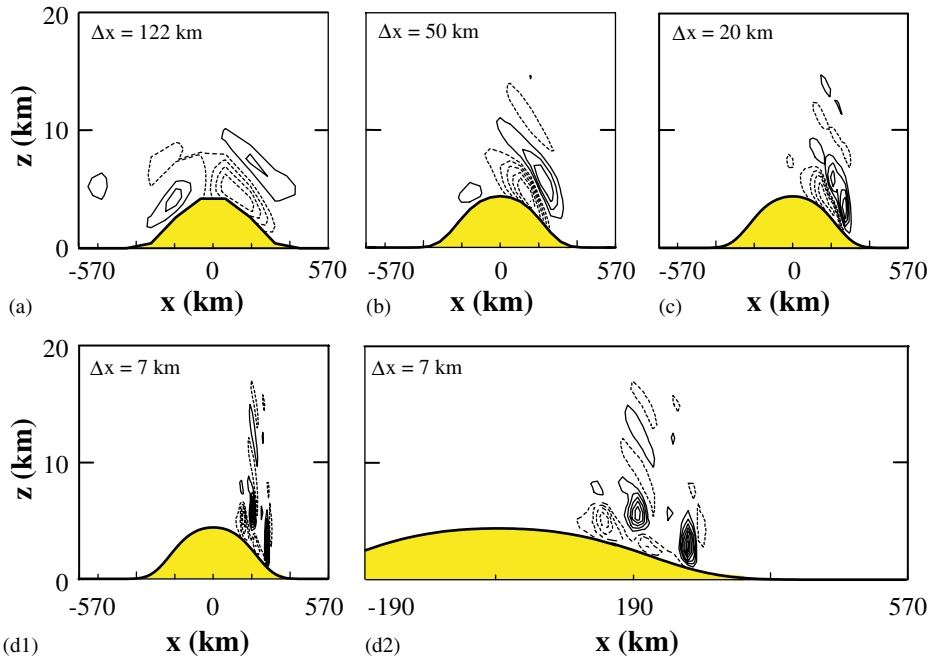

Figure 4. Vertical wind fields generated by regional simulations at 720 min: (a) simulation R2, $\Delta x = 122$ km, (min, max, inc) $= (-0.08, 0.12, 0.02)\,\mathrm{ms}^{-1}$; (b) simulation R3, $\Delta x = 50$ km, (min, max, inc) $= (-0.28, 0.15, 0.05)\,\mathrm{ms}^{-1}$; (c) simulation R4, $\Delta x = 20$ km, (min, max, inc) $= (-0.4, 0.4, 0.1)\,\mathrm{ms}^{-1}$; and (d1) and (d2) simulation R5, $\Delta x = 7.0$ km, (min, max, inc) $= (-0.8, 1.4, 0.2)\,\mathrm{ms}^{-1}$. Note that Panels d1 and d2 show identical results and differ only in scale. Panels a–d1 are all depicted at same scale as Figure 2.

is complementary to the numerical GA version demonstrated in Section 3.2 of Reference [13] and is based upon the operator form in Appendix B of that study.

Figure 4 shows the effect of resolution on the wavefield as depicted by the vertical wind field after 720 min of simulated time. Panels a–c correspond to simulations R2–R4. Panels d1, d2 both correspond to simulation R5; d2 is a closeup of d1. R2 has the same zonal resolution as global simulation G3 (enhanced resolution in the neighbourhood of the topography). The overall morphology of the wavefield in Figure 4(a) corresponds reasonably well to that seen in Figure 2(b). It displays zonal and vertical wavelengths of $\lambda_x \simeq 500$ km and $\lambda_z \simeq 8$ km—a credible match to Figure 2(b) given the approximations involved with respect to determining the local environmental state—which is *crucial* in selecting which waves out of those permitted by the dispersion relation are expressed. Not shown is the result from simulation R1, which has the same resolution as global simulation G2 (uniform grid). Those results fail to show any well developed wave fields. Panels a–d1 in Figure 4 show that the waves appear to steepen dramatically as resolution increases. Simultaneously, the magnitudes of the vertical velocity increase by a factor of $\sim 20\times$ (Simulation R2 vs R5); and the large-scale structure of the wavefield breaks up into a series of smaller wavetrains. The 3D simulation R10 is closest to the 2D simulation R5. Although not shown, it gives results that are quite similar to those in

Copyright © 2005 John Wiley & Sons, Ltd.

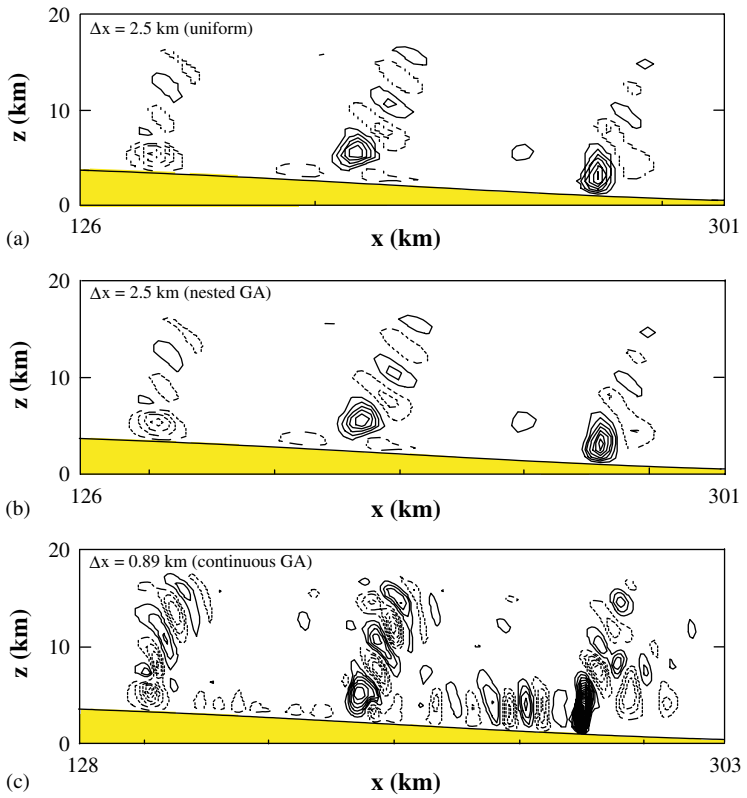

Figure 5. Vertical wind fields generated by high resolution regional simulations at 720 min: (a) simulation R6, $\Delta x = 2.5$ km (uniform), (min, max, inc) $= (-2.0, 3.2, 0.5)\,\mathrm{ms}^{-1}$; (b) simulation R7, $\Delta x = 2.5$ km (nested GA), (min, max, inc) $= (-2.0, 3.5, 0.5)\,\mathrm{ms}^{-1}$; and (c) simulation R9, $\Delta x = 0.89$ km (continuous GA), (min, max, inc) $= (-3.0, 9.0, 0.5)\,\mathrm{ms}^{-1}$.

Figure 4(d2) except that the most intense vertical updraft on the extreme right is much weaker. This is due to strong spanwise activity that cannot occur in the 2D simulations. Such affects are highly localized and although important to the details of fine scale wave interactions/turbulence, do not appear to significantly affect the overall evolution of the wavefield.[21]

Figure 5 shows a closeup of the resulting wavetrains on the downslope surface for higher resolution simulations than in Figure 4. Panels a, b correspond to simulations R6, R7. The first has a uniform resolution $\Delta x = 2.50$ km, while R7 uses the nested GA mapping (19) to achieve the same resolution in the region shown in Figure 5 but with only 36% as many gridpoints. The same timestep is used in R7 as in R6 as this is set by Courant number limitations in the target region. Nevertheless, simulation R7 takes only 22% as much CPU time to complete as does R6, substantially better than would be anticipated based upon the number of gridpoints alone. This may be due to the improvement in the condition number of the elliptic solver

[21] A similar conclusion was obtained for deep gravity wave breaking with 2D forcing [41].

Copyright © 2005 John Wiley & Sons, Ltd.

that occurs with fewer grid points. Not shown are the results from simulation R8, which uses continuous GA to achieve 2.5 km resolution in the target area. This result appears extremely similar to those shown in Panels a, b of Figure 5; simulation R8 is even faster in execution time than R7. Additional comparisons with the potential temperature and zonal wind fields of R6 fail to show any obvious wave refraction/reflection effects for R7, R8. For the nested grid example R7 this result is especially striking, although consistent with the NFT advected nested grid example of Reference [13], because of its abrupt changes in metric coefficients. We attribute this accuracy to the simultaneous use of the NFT solver MPDATA and the exacting tensor formalism of the model. Figure 5(c) shows results from simulation R9, which uses continuous GA to achieve a maximum resolution of 0.89 km in the target region using the same number of grid points as R6. The columnar nature of the wavetrains is essentially the same as shown in Panels a, b, but it is more intense and shows additional structure at finer scales—trends that are consistent with increases in resolution. Since these wave columns are only beginning to be resolved in Figure 4(d2), it appears that $\Delta x = 2.5$ km is the minimum sufficient to resolve their 'converged' structure.

In Figure 5(c) the vertical winds are $\sim 10\,\mathrm{ms}^{-1}$. This far exceeds what is allowed for hydrostatic approximations, and clearly indicates that nonhydrostatic effects are strong. This is also indicated by the aspect ratios of the columnar waves, with $\lambda_x/\lambda_z \simeq (45\,\mathrm{km})/(15\,\mathrm{km}) = 3$. This is close to the unit aspect ratio for breaking nonhydrostatic waves in References [18, 41]. The wave columns are arranged with a wavelength of $\simeq 60$ km, and weaken so strongly with height as to die out completely well below 20 km altitude. This wavefield may result from an interference pattern between the larger-scale (hydrostatic) waves depicted at lower resolution and a series of higher mode vertical waves that arise due to nonhydrostatic wave trapping [42]. The strong shear in the zonal wind throughout much of the regional atmosphere at $-35.5°$ latitude produces an environment that is conducive for wave trapping.

We conclude our discussion of the regional simulation results by returning to the initial question that motivated the regional simulations, how well must the idealized Andes be resolved in the global simulation in order to get the gravity wave forcing effect on climate correct? To gauge the wave-forcing effect, we examine the vertical component of the eddy flux (EF), $\langle \rho_b u' w' \rangle$, depicted in Figure 6. Except for result GG explained below, the averaging regions for the EF are equal to the horizontal extent of the regional domain. Broadly, simulations R2–R10 all have the same qualitative form, and R6–R10 are even in close agreement quantitatively.[22] In particular, simulation R2 which matches the enhanced zonal resolution of global simulation G3 has a qualitatively correct form for the EF. However, it does have the smallest magnitude of all the simulations in this group. Regional simulation R1, which matches the uniform zonal resolution of global simulation G2 has the wrong qualitative form and can summarily be discarded as having inadequate resolution. A regionally averaged EF from G3 at day 299.00 is also shown in Figure 6 and labelled as result GR.[23] The globally averaged EF of G3 is also shown in Figure 6 as result GG. Result GR should match R2. Instead, it matches better with the higher resolution regional simulations. In order to assess the quantitative agreement, we introduce the column integrated EF, I_{EF}. Values of I_{EF} for the

[22]This consistent trend suggests that the localized nonhydrostatic effects so prevalent at the higher resolutions do not greatly affect regionally averaged quantities.

[23]The regionally averaged eddy flux GR corresponds to a region extending 35° in longitude and 6° in latitude centred on the NS ridge of the topography at $-35.5°$ latitude.

Copyright © 2005 John Wiley & Sons, Ltd.

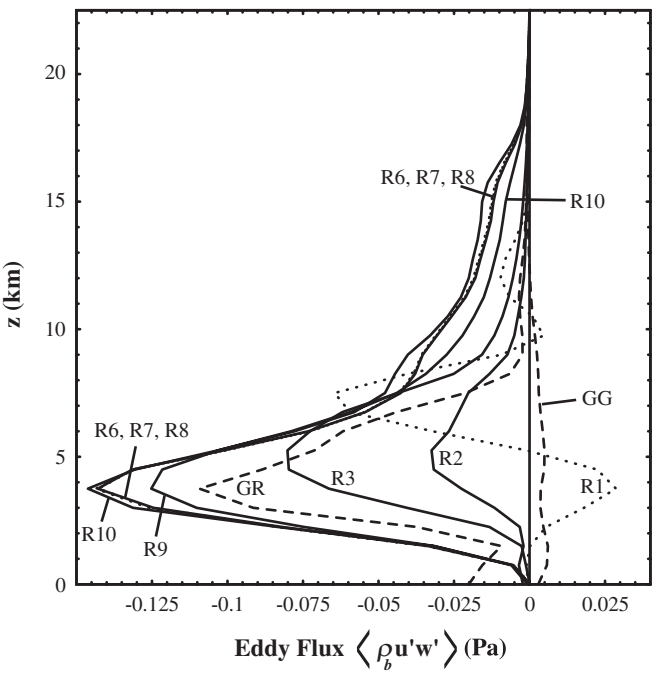

Figure 6. Vertical eddy fluxes. Regional simulations R1–R10 are evaluated at 720 min; results GR and GG are evaluated from simulation G3 at 299.00 days; GR is based upon a regional averaging extending 35° in longitude and 6° in latitude centred on the NS ridge of the topography but at −35.5° latitude; GG is based upon averaging around the whole planet.

regional simulations are listed in the last column of Table II. The integrated flux for GR is $-0.44\,\mathrm{Jm}^{-2}$, nearly three times the value of $-0.165\,\mathrm{Jm}^{-2}$ for case R2. Why such a large difference? The wavefield in global simulation G3 has been integrated throughout the duration of the transient wave event shown maximally in Figure 2, which had a time scale of ∼2 days. If one examines the transient development of I_{EF} for case R2, it is found to decrease to $-0.40\,\mathrm{Jm}^{-2}$ after 2.0 days—a much better match. We conclude that the two global simulations G2 and G3 are consistent with the regional simulations and that only G3 has sufficient resolution to get the orographic wave forcing approximately correct. Regional simulations in two other zonal bands (bounded in latitude) near the mountain peak and in the equatorial region extend this conclusion to these other two bands as well.

To assess the impact of resolved wave forcing on 'climate', a final diagnostic was utilized whereby we compared the EF's computed in several zonal bands using the results from global simulations G1–G3. Centred on the mid-latitude jets, the equatorial zone, and at −35.5°, EF's were computed in these bands using a global zonal average ($0 \leqslant \lambda \leqslant 360°$) to show the climate; and also for simulations G2, G3 a regional zonal average of 35° longitudinal extent centred on the topography to show the local wave forcing. The outstanding result is that the regional EF due to gravity waves, whether properly resolved or not, has only small impact on the climate in all zonal bands *except* the equatorial zone. We attribute this to baroclinicity. At higher latitudes, the contribution to EF by baroclinic instability dwarfs any contributions

Copyright © 2005 John Wiley & Sons, Ltd.

due to gravity waves.[24] Near the equator, however, baroclinicity vanishes and the resulting globally averaged EF field is near zero. Here regional EF's induced by orographically forced waves can impact the global average; in our study insufficient resolution causes the spurious generation of a large regional EF that results in an anomalous global jet.

4. CONCLUSIONS

Our experience to date is that MPDATA is well suited for GA, particularly within the context of continuous mapping methods. The computational model resulting from this synergism, *EULAG*, has the capability to maintain conservative properties over an extended integration period, even with GA 'turned on'. We attribute this capability to: (i) the rigor of the tensor analysis underlying the formulation—further developed in this study in regards to the *geometric conservation law* and attendant identities; and (ii) the NFT character of MPDATA. Solutions generated with *EULAG* maintain conservation and do not show Gibbs oscillations even with step changes in grid resolution—an extreme test given the assumed C^2 continuity of the coordinate mapping.

We find that by using GA to generate high resolution in targeted regions of interest, that reductions of up to an order of magnitude in CPU time appear possible compared to simulations using grids with equally high but uniform resolution. When GA vs uniform grids of the same size are examined, we find that the GA machinery itself adds only a minor cost to the computations [13]. Instead, the CPU time is dictated by physical considerations, e.g. the Courant number may increase due to better resolved or entirely new physical effects, such as nonhydrostaticity, and one has to 'pay' to sample the enhanced variability of fields in the targeted region. Conversely, if the limiting Courant number is not significantly changed in the targeted region, it is entirely possible for a simulation with GA to take *less* CPU time due to improvements in the condition number of the pressure solver.

Finally, we document that by using GA in a global model, it is possible to resolve regional episodic gravity wave forcing due to topography that would otherwise not be readily resolvable; and that failure to properly resolve such forcing can impact 'climate'. This assertion is strongly supported by a series of careful diagnostics of eddy forcing in the global simulations and in a series of regional simulations designed to elucidate the effects of model resolution on topographically forced waves.

ACKNOWLEDGEMENTS

This work was supported by U.S. Department of Energy grants DEFG0296ER61473 and DEFG0201ER63250. Computer support was provided partly by the U.S. National Center for Atmospheric Research, sponsored by the U.S. National Science Foundation. We also thank the anonymous Reviewer whose comments improved the quality of this manuscript.

[24]This is true only in the lower atmosphere. In the upper atmosphere (above 50 km), gravity wave breaking can become a major contributor to EF's and the general circulation [18].

Copyright © 2005 John Wiley & Sons, Ltd.

REFERENCES

1. Uliasz MU. Subgrid-scale parameterizations. In *Mesoscale Modeling of the Atmosphere*, Pielke RA, Pearce RP (eds). American Meteorological Society: Boston, 1994; 13–19 (Chapter 2).
2. Rodean HC. Parameterizations of turbulence statistics for model inputs. *Stochastical Lagrangian Models of Turbulent Diffusion*. American Meteorological Society: Boston, 1996; 59–64 (Chapter 12).
3. Grabowski WW. Toward cloud resolving modeling of large-scale tropical circulations: a simple cloud microphysics parameterization. *Journal of the Atmospheric Sciences* 1998; **55**:3283–3298.
4. Straka JM. Representing moisture processes in mesoscale numerical models. In *Mesoscale Modeling of the Atmosphere*, Pielke RA, Pearce RP (eds). American Meteorological Society: Boston, 1994; 29–38 (Chapter 4).
5. Smolarkiewicz PK, Margolin LG, Wyszogrodzki AA. A class of nonhydrostatic global models. *Journal of the Atmospheric Sciences* 2001; **58**:349–364.
6. Davis T, Staniforth A, Wood N, Thuburn J. Validity of anelastic and other equation sets as inferred from normal-mode analysis. *Quarterly Journal of the Royal Meteorological Society* 2003; **129**:2761–2775.
7. Durran DR. *Numerical Methods for Wave Equations in Geophysical Fluid Dynamics*. Springer: Berlin, 1999.
8. Adams J. Recent enhancements in MUDPACK, a multigrid software package for elliptic partial differential equations. *Applied Mathematical Computation* 1991; **43**:79–93.
9. Crowley J. SCE community speaks out in policy arena 2004. *SIAM News* 2003; **37**:2–3.
10. Epstein PR, McCarthy JJ. Assessing climate stability. *Bulletin of the American Meteorological Society* 2005; **85**:1863–1870.
11. JEANNE graphics archive. National Weather Service Tropical Prediction Center, National Hurricane Center, http://www.nhc.noaa.gov/archive/2004/JEANNE_graphics.shtml (27 February 2005).
12. Iselin JP, Gutowski WJ, Prusa JM. Tracer advection using dynamic grid adaptation and MM5. *Monthly Weather Review* 2005; **133**:175–187.
13. Prusa JM, Smolarkiewicz PK. An all-scale anelastic model for geophysical flows: dynamic grid deformation. *Journal of Computational Physics* 2003; **190**:601–622.
14. Smolarkiewicz PK, Prusa JM. Toward mesh adaptivity for geophysical turbulence: continuous mapping approach. *International Journal for Numerical Methods in Fluids* 2005; **47**:789–801.
15. Fox-Rabinovitz MS, Suarez MJ, Takacs LL. A finite-difference GCM dynamical core with a variable-resolution stretched grid. *Monthly Weather Review* 1997; **125**:2943–2968.
16. Gal-Chen T, Somerville CJ. On the use of a coordinate transformation for the solution of the Navier–Stokes equations. *Journal of Computational Physics* 1975; **17**:209–228.
17. Sharman RD, Keller TL, Wurtele MG. Incompressible and anelastic flow simulations on numerically generated grids. *Monthly Weather Review* 1988; **116**:1124–1136.
18. Prusa JM, Smolarkiewicz PK, Garcia RR. On the propagation and breaking at high altitudes of gravity waves excited by tropospheric forcing. *Journal of the Atmospheric Sciences* 1996; **53**:2186–2216.
19. Bacon DP *et al.* A dynamically adapting weather and dispersion model: the operational multiscale environmental model with grid adaptivity (OMEGA). *Monthly Weather Review* 2000; **128**:2044–2076.
20. Thompson JF, Thames FC, Mastin CW. Automatic numerical generation of body-fitted curvilinear coordinate system for field containing any number of arbitrary two-dimensional bodies. *Journal of Computational Physics* 1974; **15**:299–319.
21. Thomas PD, Lombard CK. Geometric conservation law and its application to flow computations on moving grids. *AIAA Journal* 1979; **17**:1030–1037.
22. Ghia KN, Ghia U (eds). *Advances in Grid Generation*. The American Society of Mechanical Engineers: New York. *Applied Mechanics*, *Bioengineering*, *and Fluids Engineering Conference*, vol. FED-5. Houston, TX, 20–22 June 1983.
23. Prusa JM, Yao LS. Effects of density change and sub-cooling on the melting of a solid around a horizontal heated cylinder. *Journal of Fluid Mechanics* 1985; **155**:193–212.
24. Kassinos AC, Prusa JM. A numerical model for 3-D viscous sloshing in moving containers. In *Recent Advances and Applications in Computational Fluid Dynamics*, Baysal O (ed.). The American Society of Mechanical Engineers: New York. *Winter Annual Meeting*, vol. FED-103. Dallas, TX, 25–30 November 1990; 75–86.
25. Wedi NP, Smolarkiewicz PK. Extending Gal-Chen & Somerville terrain-following coordinate transformation on time-dependent curvilinear boundaries. *Journal of Computational Physics* 2004; **193**:1–20.
26. Dietachmayer GS. Application of continuous dynamic grid adaptation techniques to meteorological modeling. Part II: efficiency. *Monthly Weather Review* 1992; **120**:1707–1722.
27. Fiedler BH, Trapp RJ. A fast dynamic grid adaptation scheme for meteorological flows. *Monthly Weather Review* 1993; **121**:2879–2888.
28. Iselin JP, Prusa JM, Gutowski WJ. Dynamic grid adaptation using the MPDATA scheme. *Monthly Weather Review* 2002; **130**:1026–1039.
29. Smolarkiewicz PK, Margolin LG. MPDATA: a finite difference solver for geophysical flows. *Journal of Computational Physics* 1998; **140**:459–480.

Copyright © 2005 John Wiley & Sons, Ltd.

30. Smolarkiewicz PK, Pudykiewicz JA. A class of semi-Lagrangian approximations for fluids. *Journal of the Atmospheric Sciences* 1992; **49**:2082–2096.
31. Prusa JM, Smolarkiewicz PK. Dynamic grid deformation: continuous mapping approach. *Proceedings ECMWF Seminar on Recent Developments in Numerical Methods for Atmospheric and Ocean Modeling*, ECMWF: Reading, U.K., 6–10 September 2004; 267–283.
32. Lipps FB, Hemler RS. A scale analysis of deep moist convection and some related numerical calculations. *Journal of the Atmospheric Sciences* 1982; **39**:2192–2210.
33. Smolarkiewicz PK, Prusa JM. Forward-in-time differencing for fluids: simulation of geophysical turbulence. In *Turbulent Flow Computation* Drikakis D, Guertz BJ (eds). Kluwer Academic Publishers: Dordrecht, 2002; 207–240.
34. Smolarkiewicz PK, Grubišić V, Margolin LG. On forward-in-time differencing for fluids: stopping criteria for iterative solutions of anelastic pressure equations. *Monthly Weather Review* 1997; **125**:647–654.
35. Skamarock WC, Smolarkiewicz PK, Klemp JB. Preconditioned conjugate-residual solvers for Helmholtz equations in nonhydrostatic models. *Monthly Weather Review* 1997; **125**:587–599.
36. Smolarkiewicz PK, Margolin LG. Variational solver for elliptic problems in atmospheric flows. *Applied Mathematics and Computer Science* 1994; **4**:527–551.
37. Farhat C, Geuzaine P, Grandmont C. The discrete geometric conservation law and the nonlinear stability of ALE schemes for the solution of flow problems on moving grids. *Journal of Computational Physics* 2001; **174**:669–694.
38. Synge JL, Schild A. *Tensor Calculus*. Dover: New York, 1978.
39. Held IM, Suarez MJ. A proposal for intercomparison of the dynamical cores of atmospheric general circulation models. *Bulletin of the American Meteorological Society* 1994; **75**:1825–1830.
40. Randel WJ. Global atmospheric circulation statistics, 1000-1 mb. *NCAR TN-266+STR*, National Center for Atmospheric Research, Boulder, CO, 1992.
41. Prusa JM, Smolarkiewicz PK, Wyszogrodzki AA. Simulations of gravity wave induced turbulence using 512 PE CRAY T3E. *International Journal of Applied Mathematics and Computer Science* 2001; **11**:101–115.
42. Keller TL. Implications of the hydrostatic assumption on atmospheric gravity waves. *Journal of the Atmospheric Sciences* 1994; **51**:1915–1929.

Copyright © 2005 John Wiley & Sons, Ltd.